Investigations on offshore wind turbine inflow modelling using numerical weather prediction coupled with local-scale computational fluid dynamics

Alessio Castorrini[a,*], Sabrina Gentile[b,c], Edoardo Geraldi[b], Aldo Bonfiglioli[a]

[a] *School of Engineering, Università della Basilicata, Viale dell'Ateneo Lucano 10, 85100 Potenza, Italy*
[b] *CNR Italian National Research Council - IMAA C.da S.Loja - 85020 Tito Scalo (PZ), Italy*
[c] *Center of Excellence Telesensing of Environment and Model Prediction of Severe events (CETEMPS), University of L'Aquila, 67100 L'Aquila, Italy*

Abstract

The computational power available nowadays to industry and research paves the way to increasingly more accurate systems for the wind resource prediction. A promising approach is to support the mesoscale numerical weather prediction (NWP) with high fidelity computational fluid dynamics (CFD). This approach aims at increasing the spatial resolution of the wind prediction by not only accounting for the complex and multiphysics aspects of the atmosphere over a large geographical region, but also including the effects of the fine scale turbulence and the interaction of the wind flow with the sea surface. In this work, we test a set of model setups for both the mesoscale (NWP) and local scale (CFD) simulations employed in a multi-scale modelling framework. The method comprises a one-way coupling interface to define boundary conditions for the local scale simulation (based on the Reynolds Averaged Navier-Stokes equations) using the mesoscale wind given by the NWP system. The wind prediction in an offshore site is compared with LiDAR measurements, testing a set of mesoscale planetary boundary layer schemes, and different model choices for the local scale simulation, which include steady and unsteady approaches for simulation and boundary conditions, different turbulence closure constants, and the effect of the wave motion of the sea surface. The resulting wind is then used for the simulation of a large wind turbine, showing how a realistic wind profile and an ideal exponential law profile lead to different predictions of wind turbine rotor performance and loads.

Keywords: wind, mesoscale, RANS, WRF, NWP, PBL, wind energy, wind turbine

1. Introduction

With the continuous growth of computing power resources, downscaling techniques which use computational fluid dynamics (CFD) to increase the spatial resolution of numerical weather predictions (NWP) is now often applied by the researchers in wind applications (a significant example is the work done for the European Wind Atlas [1]).

A wide literature can be found on the meso/local-scale simulation coupling techniques and interface modelling, with applications ranging from the pollutant transport [2; 3], evaluation of wind and wind loads in urban areas [4; 5; 6], and wind energy. Focusing on the wind energy, the approach improves the capability to support (or avoid) the need

*Corresponding author. e-mail: alessio.castorrini@unibas.it

for wind measurement to assess the wind resource or predict the incoming wind inflow on a wind farm installation site. This capability becomes even more interesting when the target application is offshore, where new measurement are expensive and historical measurements often unavailable. Multi-scale approaches can improve the fidelity of the wind inflow models used in the mechanical simulation of wind turbines. This is particularly true because new wind turbine models up to 15 MW of rated power are going to be the edge of the future industrial production, and the classical assumption of straight wind with uniform turbulence intensity is questionable if applied to these scales. Indeed, 15 MW turbines can have rotors up to 240 m in diameter, with the blade tips reaching 300 m of elevation above the ground [7]. Such rotors cover much of the planetary boundary layer (PBL), and features such as strong wind veer (vertical variation of the wind direction), non uniform turbulent scales, and non-neutral wind velocity profile are expected in this elevations range.

There are many possible model frameworks and approaches presented in the literature, and the best choice depends on the target application. Durán et al. [8; 9] used the averaged results from mesoscale NWP and local-scale simulations based on the steady Reynolds Averaged Navier-Stokes (RANS) equations to perform annual wind resource assessment over a set of locations with complex terrains. A method for wind resource assessment based on averaged NWP results and RANS was proposed also by Duraisamy et al. [10], while an automatic approach based on time-averaged snapshots of the NWP data obtained from operational forecasting was proposed by Castorrini et al. in [11] and applied to increase the spatial accuracy of the wind prediction on an onshore site with complex terrain. More computationally demanding solutions, based on time-dependent simulations, include the use of Unsteady RANS [12; 13] and Large Eddy Simulation (LES) on the local-scale side [14; 15]. However, these latter approaches imply a considerable demand of computational resources to get completely developed wind fields over the large domains under scrutiny. Therefore, a widely used approach is to use the mesoscale simulation to define the boundary conditions for a steady or unsteady RANS solver based on standard two equations turbulence closure, adapted for PBL applications (as presented in Section 2). This approach allows for limited computational costs especially when a steady solver is employed for the local-scale simulation. In this work, the approach defined in [11] is taken as a reference base to build the multiscale framework.

A large body of literature exists about adaptation, correction, and verification of RANS and eddy viscosity models in the simulation of the PBL in neutral and non-neutral conditions. Among others we recall the model adaptations proposed by Richards et al. [16], Bechmann et al. [17], Katul et al. [18], Sogachev et al. [19], Detering et al. [20]. An extensive and rigorous work has been conducted by Temel et al. [21; 22] particularly dedicated to establish consistent adaptation of the RANS closures for CFD simulation gaining the inflow boundary conditions from the mesoscale model. All the aforementioned works have been used as a guideline for setting the best options for the local-scale turbulence modelling used in the present work; this will be reported with more details in Section 2 and 3.

Work can still be done on the verification of accuracy and limits of the downscaling techniques, because of the wide variability of wind conditions in the PBL. The accuracy of the final prediction depends on the model choices made on both sides of the multiscale approach. It will be shown that the same choices that give a good result for a certain wind condition may not be the best option for other conditions taken at the same location, but at a different time of the day. The present paper shows the capabilities and quantifies some uncertainties associated with a set of model choices that

can be made in the definition of the multiscale framework.

The sample application presented here consists in applying the downscaling to the prediction of the wind in an offshore site taking two different time snapshots in a day extracted from the LiDAR measurement campaign of FINO2 [23], which collects measurements of the wind profile taken every 10 minutes from July 2011 to July 2012. The measurements are compared against the results obtained using different settings used in the two scales simulations setup. Focus is put on the meso/local-scale interface in terms of boundary conditions, PBL schemes in the mesoscale simulation, turbulence closure models, and turbulence model constants in the local-scale simulation. Another aspect studied here is the influence of the sea waves and unsteady aerodynamics on the simulated boundary layer profile. In this paper, this aspect will be accounted with a dynamic morphing of the computational domain. Finally, the wind prediction obtained from the proposed multiscale method is used to estimate the rotor power and loads of the IEA 15MW wind turbine [7], by comparison with the performance and loads arising under a turbulent wind estimated with National Renewable Energy Laboratory (NREL) TurbSim generator [24] and the theoretical power law profile.

The paper is organized starting with the description (Sec. 2) of the main models and methodologies adopted and tested in this study. Then, Sec.3 shows the design of the virtual experiment, the data used for verification and validation, and the sensitivity studies aimed at assessing the grid independence of the results. Sec. 4 reports the results of the study and the comparisons of the wind predictions obtained by the different setups and models outlined in Sec. 3 and 2, followed by a sample simulation of a large wind turbine using the final result of the wind prediction.

2. Material and methods

2.1. Mesoscale simulation and PBL schemes

The mesoscale wind prediction is obtained using WRF-ARW, an open source NWP system designed for multiple purposes ranging from operational forecasting to sophisticated atmospheric studies. The WRF-ARW core system, developed through the collaboration of several research institutes headed by the National Center for Atmospheric Research (NCAR, `http://www.wrfmodel.org`), solves the Eulerian fully compressible non-hydrostatic equations, using a mass vertical coordinate varying with the height. The solution is obtained on a staggered Arakawa-C grid, and the local resolution on specific areas can be increased with horizontal nesting (one or two-way). The multi-physics parameterizations include options for cumulus convection, microphysics, radiation, planetary boundary layer and land-surface modelling [25; 26; 27]. These features enable the WRF-ARW system to cover a wide range of different applications in the green energy area, ranging from solar irradiance [28; 29; 30; 31; 32] to wind energy prediction [33; 34; 35].

When adopted for wind resource prediction, WRF-ARW is generally used with maximum horizontal resolutions of the order of a few kilometers (2-5 km). Although this horizontal resolution is not sufficient for an accurate prediction of the wind field over an on-shore site with complex terrain [11], it can provide accurate predictions of the offshore wind far from land, where aspects such as thermal convection, stratification and dynamics of the PBL on large scales are dominant with respect to the ground effects. The WRF-ARW system offers several choices to model the PBL using

different schemes. In this work, the mesoscale simulation has been performed using different PBL parameterizations, comparing the wind vertical profile in the first 300 m above the sea level with the measurements.

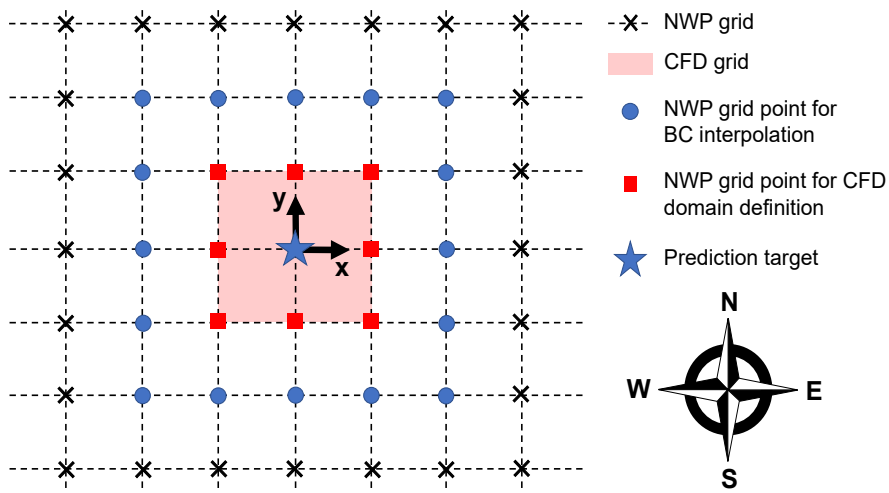

Figure 1: Mesoscale and local-scale domains configuration and interface interpolation points.

2.2. *Local-scale simulation*

In the present work, the local-scale model consists in the incompressible RANS equations, steady and unsteady. Turbulence closure relies on the two equations k-ε and k-ω models.

Stratification and stability (diurnal cycle) effects related to the vertical temperature profile are accounted for using the Boussinesq approximation [36], which states that the density variation has non-negligible effect only in relation to the gravitational acceleration. This approach allows to retain the incompressible model (and the associated solvers), and to reduce the energy equation to the temperature transport equation.

The final system of governing equation can be written as:

$$\boldsymbol{\nabla}\cdot(\rho\boldsymbol{U}) = 0 \tag{1}$$

$$\frac{\partial(\rho\boldsymbol{U})}{\partial t} + \boldsymbol{\nabla}\cdot(\rho\boldsymbol{U}\otimes\boldsymbol{U}) - \boldsymbol{\nabla}\cdot\left[2(\mu+\mu_t)(\boldsymbol{\nabla}\boldsymbol{U}^T + \boldsymbol{\nabla}\boldsymbol{U})\right] + \boldsymbol{\nabla}P + \boldsymbol{S}_G + \boldsymbol{S}_C + \boldsymbol{S}_P = 0 \tag{2}$$

$$\frac{\partial T}{\partial t} + \boldsymbol{\nabla}\cdot(T\boldsymbol{U}) - \boldsymbol{\nabla}\cdot[(\alpha+\alpha_t)\boldsymbol{\nabla}T] = 0 \tag{3}$$

$$\frac{\partial(\rho k)}{\partial t} + \boldsymbol{\nabla}\cdot(\rho k\boldsymbol{U}) - \boldsymbol{\nabla}\cdot(D_k\boldsymbol{\nabla}k) - P_k + B_2 - P_G = 0 \tag{4}$$

$$\frac{\partial(\rho\varepsilon)}{\partial t} + \boldsymbol{\nabla}\cdot(\rho\varepsilon\boldsymbol{U}) - \boldsymbol{\nabla}\cdot\left(\frac{\mu_t}{\sigma_\varepsilon}\boldsymbol{\nabla}\varepsilon\right) - \frac{\varepsilon}{k}(C_1P_k - C_2\rho\varepsilon + C_3P_G) = 0 \tag{5}$$

$$\frac{\partial(\rho\omega)}{\partial t} + \boldsymbol{\nabla}\cdot(\rho\omega\boldsymbol{U}) - \boldsymbol{\nabla}\cdot[(\mu+\sigma_\omega\mu_t)\boldsymbol{\nabla}\omega] - \frac{\omega}{k}(C_1P_k - C_2\rho\omega k + C_3P_G) = 0 \tag{6}$$

adopting either Eq. 5 or Eq. 6 as second equation for the k-ε or k-ω turbulence closure. In the equations above, $\boldsymbol{U}$, P and T are the Reynolds averaged flow velocity, pressure and temperature; k is the turbulent kinetic energy (TKE), ε the TKE dissipation rate, and $\omega = \varepsilon/k$ is the specific TKE dissipation rate. ρ, μ and $\alpha = \nu/Pr$ are the fluid density, viscosity and thermal diffusivity ($\nu = \mu/\rho$). The definition of the eddy viscosity ν_t, of the eddy thermal diffusivity $\alpha_t = \nu_t/Pr_t$, and of the model constants (D_k, C_1, C_2, C_3), depends on the turbulent closure model adopted. For the case

of standard k-ε [37], $\mu_t/\rho = C_\mu k^2/\varepsilon$ and (D_k, C_μ, σ_k, σ_ε, C_1, C_2, C_3) = (μ_t/σ_k, 0.09, 1.0, 1.3, 1.44, 1.92, 0.0), while for the k-ω SST model [38] $\mu_t = a_1 k/max(a_1\omega, F_2 S)$ and (D_k, C_μ, σ_k, σ_ε, C_1, C_2, C_3) = ($\mu + \mu_t\sigma_k$, 0.09, 1.0, 1.3, 1.44, 1.92, 0.0). Following [21], the turbulent Prandtl number Pr_t can be set to 1.16, 1.0, and 0.9 respectively for stable, neutral and unstable conditions.

In addition to the buoyancy effects, when simulating atmospheric flows, additional source and sink terms are added to the set of RANS and closure equations, to account for: Earth rotation, ambient turbulence, and geostrophic wind drag. In eq. 2, $\boldsymbol{S}_G = \rho\mathbf{g}\left[1-\beta(T-T_{ref})\right]$ is the momentum source associated with buoyancy effects, β and $\mathbf{g}$ being the thermal expansion coefficient and the gravitational acceleration vector respectively. $\boldsymbol{S}_C = \rho 2(\boldsymbol{\Omega}\times\boldsymbol{U})$ is the Coriolis force term, $\boldsymbol{\Omega}$ being the Earth angular velocity. $\boldsymbol{S}_P$ is the additional source term (given in form of a driving pressure gradient) to account for the geostrophic wind drag. The buoyancy effect is also accounted for in the turbulence models by the term $P_G = \rho\frac{\beta\mu_t(\boldsymbol{\nabla}T\cdot\mathbf{g})}{Pr_t}$ [39].

As outlined in [40], the eddy viscosity models are single-length-scale models that set the mixing length equal to the dissipation length. As a consequence, in a PBL simulation, the turbulence length scale grows almost linearly with the height. In order to correct this aspect, a source term is added to the ε or ω equation, with the aim of limiting the length scale to a maximum value appropriately chosen on the basis of the Obukhov length L for stably stratified PBL ($l_{max} \approx 0.08L$), or on the basis of PBL height h for unstable conditions ($l_{max} \approx h/3$).

Wall functions are generally applied in the RANS simulation of PBL, to account for the effect of ground roughness and thermal gradients. As noted in [41] and remarked in [42], when RANS models are adopted in their standard formulation, the rough wall treatment based on standard wall functions and equivalent roughness length may lead to y^+ values at the first cell above the ground, which are far from the range assumed for the standard log law. Modifications have been proposed to maintain the proper k-profile for a range of roughness heights much larger than in standard RANS applications. Possible ways to improve the treatment of k and ε within the cells close to the ground have been given, for example, in [16] or [22]. In this study, we apply the model implemented in openFoam and based on [42], taking care to prepare local-scale grids which fulfil the requirement of having $30 < y^+ < 300$ in all simulations.

The roughness length to be set for the water surface depends on wind speed and waves spectrum. Because of the high wind velocities, the roughness length z_0 is estimated in this study using Charnock's relation $z_0 = a_C u_\star^2/g$ [43], where $u_\star$ is the friction velocity and g is the magnitude of the gravitational acceleration. The Charnock's constant can be estimated empirically ($a_C = (1\pm 0.2)\times 0.016$), or by a relation that accounts for the wave age $c_0/u_\star$ (where c_0 is the phase speed of the peak wave). An alternative formula is given for example in [44], where $a_C = \frac{1}{2}\left(\frac{c_0}{u_\star}\right)^2 \exp(-\frac{\kappa}{B}\frac{c_0}{u_\star})$. In the last relation, B is a proportionality constant between c_0 and the surface relative wind speed, and κ is the von Karman's constant. Charnock's relation has been proved to be accurate for winds over the ocean having 4 to 50 m/s of velocity at 10 m above the sea. Applying the Charnock's relation to the range 5 to 10 m/s of wind velocity, a $z_0 = 0.1-1$ mm is obtained, suggesting that even large waves have generally less effect than a grass field on the skin friction. However, the offshore boundary layer is affected by the presence of waves, and wind-wave interaction is a complex field of study [45; 46]. A possible solution will be explored in this paper to account for the presence of waves in the unsteady local-scale simulation: the waves will be modelled as a dynamic morphing of the grid following

a prescribed motion of the sea surface. Therefore, a further model is included in the simulation framework, namely dynamic mesh morphing [47; 48], whereby the displacement of the sea surface is imposed at each time step as a boundary condition for a Laplacian solver, which propagates it through the grid nodes.

For simplicity, the waves' profile is defined using the assumption of linear wind waves having only one frequency f, wavelength λ, amplitude H_s, and propagating in the same direction of the wind. The law of sea points displacement is given then by the wave profile equation defined in [49]:

$$H(t,x,y) = H_s \cos(kx\cos\theta + ky\sin\theta - 2\pi f t + \Phi) \tag{7}$$

where H is the elevation of the water surface above the mean sea level, $k = 2\pi/\lambda$ is the wave number, θ is the angle between the x-axis and the direction of wave propagation, Φ is the phase angle, and x, y, and t are the sea surface coordinates and time respectively. According to [49], the wave length can be obtained from the dispersion equation of the component wave (wave formula associated to one wave-length), once the wave period T_s and the water depth h are given:

$$\lambda = \frac{g}{2\pi} T_s^2 \tanh \frac{2\pi h}{\lambda}. \tag{8}$$

It is worth underlining that the choice of this approach rather than a volume of fluid method (as in [48] for example), is driven by the need to keep full control of the mesh resolution inside the boundary layer near the water surface. A similar approach was adopted in [46] to perform an LES study of a marine boundary layer over non-uniform swell waves field.

2.3. Meso/local-scale interface

In this section we describe how the simulation data are passed from the meso-scale to the local-scale model, whereas the simulation results will be compared with measurement data (details in Section 3). In typical wind measurement campaigns (and also in the case presented here), the measure is averaged in time and its statistical features are collected every 10 minutes. Therefore, we can adopt as a first choice for the downscaling procedure the framework proposed in [11]. In that case, the data from mesoscale simulation is averaged over the reference time period and passed to a steady RANS simulation to increase the spatial resolution of the prediction. Velocity, turbulent kinetic energy and temperature are exported from WRF-ARW in the form of time series within a set of mesoscale grid-points (for all pressure levels) in the neighbourhood of the measurement site. Then, the data is interpolated over the boundaries of a local-scale domain surrounding the target location.

A brief discussion is given here on the selection of the local-scale domain sizes. In an offshore case, the solution given by the RANS modelling should be consistent with the mesoscale prediction for elevations above the surface layer (typically the lowest 10% of PBL). Indeed, the NWP can simulate large scales wind features and effects above the surface layer, and as it is also shown in this paper, in offshore sites the effect of the sea surface on the wind profile and turbulence is limited to a few tens of meters. Above the layer, the mesoscale simulation should be (and it proves to, see Section 4) able to predict with good accuracy the wind velocity and turbulence, and no further improvement is expected by using the local-scale model. In fact, the approach adopted here, and in most of the downscaling application studies,

is a one-way coupling whereby the mesoscale solution is used as boundary condition for the local-scale simulation. The aim is to increase the spatial resolution and include those local effects that are not sufficiently accounted in the mesoscale simulation. Differently from the usual practice, however, in the present approach, the vertical size of the CFD domain does not cover the entire PBL height and the vertical size of the first cell close to the water surface is kept of the order of few centimeters. The domain is selected with the purpose of increasing the resolution only in a small area surrounding a wind turbine or wind farm, reducing as much as possible the height of the CFD domain, and thus avoiding unnecessarily high computational costs. A sensitivity study to this parameter is presented in Section 3 showing that using the appropriate boundary conditions on the upper boundary of the CFD domain, the local-scale solution almost overlaps with the mesoscale prediction.

The lateral size is selected under similar considerations. The absence of complex terrain allows to shrink the local-scale domain and increase the resolution of the local-scale prediction just within a few cells of the mesoscale grid. Taking the target site as the center of the domain, the local-scale domain is built using the four neighbouring adjacent cells of the mesoscale grid, see Figure 1. Cubic interpolation is used to project the WRF-ARW solution over the local-scale domain boundaries. Therefore, a set of additional WRF-ARW grid-points is used to provide a sufficiently wide stencil to support cubic interpolation. Figure 1 shows the configuration taken by the mesoscale and local-scale domains, the orientation of the axes and the points of the WRF grid selected for defining the local-scale domain and interpolating the boundary conditions. To improve the resolution of the inflow velocity profile at the lateral boundaries, the log-law $u = \frac{u_*}{\kappa} \ln\left(\frac{z-z_0}{z_0}\right)$ [50] is used to prescribe the wind velocity in the first 10 m above the water surface (where WRF-ARW data are not available).

The variables extracted every time step over the selected grid points from WRF-ARW simulations are the wind velocity components, pressure, temperature, and turbulent kinetic energy.

The second turbulent closure scalar at the boundary can be obtained using the algebraic relation $\varepsilon = C_\mu^{3/4} k^{3/2}/l$, based on the mixing length $l = \left(\frac{1}{\kappa z} + \frac{1}{l_{max}}\right)^{-1}$.

The initial conditions are computed by running a precursor case with cyclic lateral boundaries, using an initial condition of uniform temperature, turbulent kinetic energy and wind velocity components, whose values are set equal to the average in space and time taken from the WRF-ARW results. The precursor run aims at initializing the internal field with a consistent vertical profile of all the variables, improving the stability of the simulation with mesoscale-derived boundary conditions in the initial iterations.

Once an optimal model has been found with steady solvers, the same set of parameters and boundary conditions have been used with the unsteady RANS (URANS) solver in order to include the effect of the flow unsteadiness. Here, the time-dependent inflow condition coming from the mesoscale is either time-averaged over the entire time-frame of the URANS simulation or used as a time-dependent boundary condition. In this latter case, a linear interpolation is adopted to project the mesoscale data to the time domain discretization used in the local-scale simulation.

3. Application

3.1. Test site and test days

All the simulations are compared with LiDAR measurements taken at the FINO2 research platform [51], and available at [23]. The wind measurements, obtained by a pulsed Leosphere Windcube v2 LiDAR, cover a one year window (from July 2012 to July 2013), providing the mean velocity, direction, turbulence intensity, variance and covariance of the wind speed every 10 minutes and for eleven altitudes (62, 72, 82, 92, 102, 120, 140, 160, 200, 240, and 280 m above sea level). The FINO2 platform is located in the Baltic Sea at 55° 00' 24.94" N, and 13° 09' 15.08" E, 35 km far from the land in any direction. This location will be referred in the following as the observation point (OP). In the present study, a representative winter day (15th of December 2012), characterised by a strong and variable wind, has been selected to test the mesoscale simulation with different PBL schemes. The measurements over the whole day are compared against the mesoscale simulations, while the measurements at two specific snapshots are extracted for the verification of the downscaling approaches. The first snapshot (h 10:30) is characterised by a velocity profile with a moderate turbulence intensity, while the second one (h 17:30) is characterised by a strong veer of the wind direction and a more unstable boundary layer condition.

3.2. Simulation campaign

The mesoscale simulations have been performed using the WRF ARW system version 4.3, released in May 2021 by NCAR [26]. The WRF-ARW model is operational since 2016 at the Institute of Methodologies for Environmental Analysis of the National Research Council (IMAA-CNR). The computational meso-scale grid is characterized by two domains nested in two-way mode. The low-resolution domain (d01, 400 × 300 cells) covers an area of 1500 squared Mm with a grid spacing of 3.6 km; the nested grid (d02, 463 × 385 cells) covers an area of 260 squared Mm around the OP and it has a resolution of 1.2 km (Figure 2). WRF-ARW uses as initial and boundary conditions the analysis at 0.125 degrees of the High Resolution (HRES) model released by the European Centre for Medium-range Weather Forecasts (ECMWF). The WRF-ARW vertical grid is common to the two domains with 40 vertical levels, ranging from the surface to the upper boundary which is set to 100 hPa. The vertical levels feature an unequally spaced distribution with the first level at approximately 10 m above the ground and a higher density (the first 15 levels) within the PBL. The time integration scheme is a third order Runge–Kutta, with a time step of 20 s for the largest domain and to 6.67 s for the finest domain.

The physics options adopted for the WRF-ARW simulations are the Thompson aerosol-aware microphysics scheme [52], the Rapid Radiative Transfer Model (RRTM) for the longwave radiation parameterization [53], the Dudhia shortwave radiation scheme [54], the revised MM5 surface layer scheme for the surface [55] and the Noah Land Surface Model for the land surface option [56]. Since the horizontal grids used in both domains is finer than 5 km, the convective motion is explicitly calculated by the model, so the cumulus parametrization is not necessary. For the simulation of the PBL dynamics have been selected all the parameterizations that include a closure equation for the TKE thus enabling the mesoscale simulation to provide more complete boundary conditions to the turbulent CFD simulation in the local-scale. The chosen PBL schemes are: Mellor–Yamada–Janjic (MYJ, A) [57], quasi-normal scale elimination (QNSE, B) [58],

Mellor–Yamada Nakanishi and Niino Level 2.5 (MYNN2.5, C) and 3.0 (MYNN3.0, D) [55], the Bougeault–Lacarrére (BOULAC, E) [59], Bretherton-Park University of Washington (UW, F) [60], Grenier-Bretherton-McCaa (GBM, G) [61], $E-\varepsilon$ (EEPS, H) [20], and 3D turbulent kinetic energy turbulent mixing scheme (3DTKE, I) [62]. Table 2 reports the list of PBL schemes tested in the mesoscale simulation campaign, identified using a letter from A to I to support the discussion of the results in Section 4.

Figure 3 shows the synoptic situation at the 00:00 UTC of 15th of December 2012. The OP area is interested by two dominant synoptic structure. In the west side there is the Siberian High-pressure: a massive ridge with a maximum value of 550 geopotential decameter (gpdm) at the isobaric surface of 500 hPa and of 1060 hPa at the surface located at the western part of the Central Siberian Plateau (Figure 3a). In the OP east side there is the deep trough of 960 hPa at the surface centered in the north Atlantic Ocean (Figure 3a). This baric configuration causes a strong southern flow (Figure 3b).

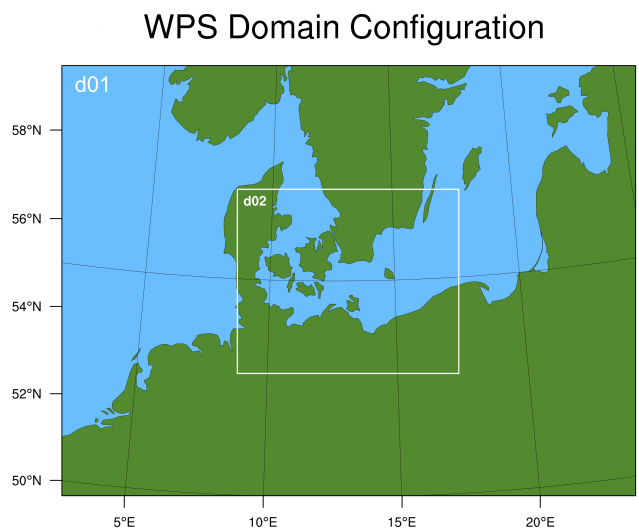

Figure 2: Position of the domains for the mesoscale simulation: d01 the mother domain with a grid spacing of 3.6 km, d02 the inner domain with 1.2 km horizontal resolution.

The definition of the local-scale domain has been given in Section 2.3. The size of the cells in the finer WRF domain leads to a horizontal size of the local-scale domain of around 4.8 km. In this study, the vertical height of the local-scale domain is set equal to the average elevation of the WRF points corresponding to the pressure level closest to h_{REF} = 600 m. This value has been chosen to be large enough to include a multi-megawatt wind turbine, and perform the downscaling of the prediction only within the range of elevations typical for wind turbine applications. As already mentioned in Section 2, in this approach and for an offshore application, the local-scale solution is expected to match the mesoscale solution above the surface layer, where the water surface effect is not felt anymore. To verify this claim, three simulations with different domain heights h_{REF} have been performed. Figure 4 reports the results of the study showing that the vertical profile, ranging between the water surface and h_{REF}, does not change significantly even if the local-scale domain height is increased above 600 m.

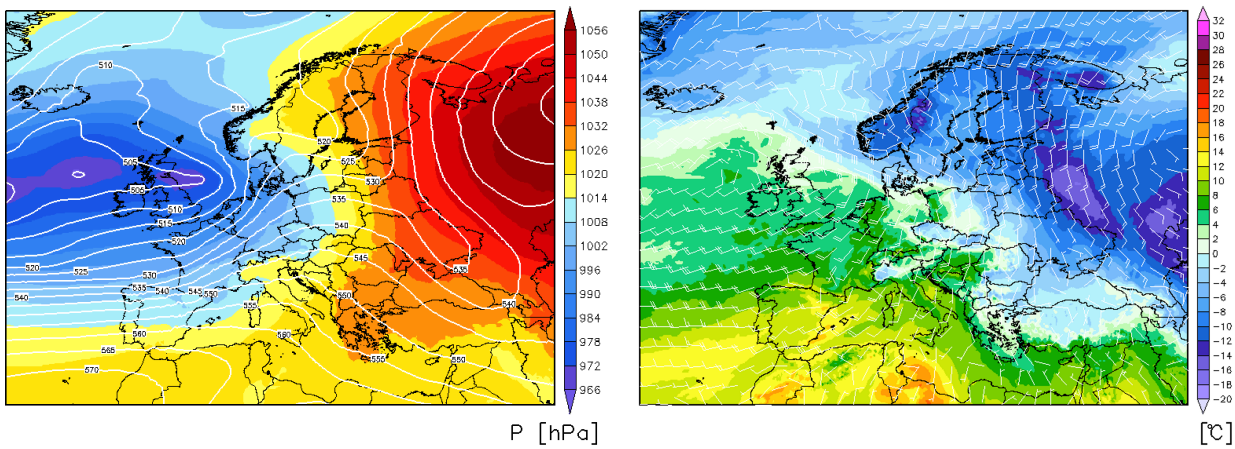

(a) 500 hPa geopotential height (white lines) and mean sea level pressure (gpdm).

(b) Wind speed (barbs) and temperature (°C) at 925 hPa.

Figure 3: Synoptic situation at the 00:00 UTC of 15th of December 2012 from the European Centre for Medium-Range Weather Forecasts (ECMWF) model.

The simulation campaign on the local-scale side went through four subsequent phases. A first verification phase is done with steady RANS simulation, starting from the averaged mesoscale field in the first snapshot. Table 3 collects the definition of the test cases for the steady simulations set, which differ by the choice of the turbulence model (k-ε or k-ω), and by the set of model constants adopted. The coefficient C_3 is set to 1.0 as suggested by [21] to improve the numerical stability. The turbulence model configuration which shows the most accurate results in phase one is then selected for the second phase. Here, the unsteady RANS simulation is performed using both time-averaged and time dependent inflow boundary conditions coming from the mesoscale simulation. The time dependent simulation runs for the 10 minutes time window of the first snapshot. The same turbulence model configuration selected in phase one is then used in phase three to run an unsteady simulation considering either time-averaged or time dependent inflow boundary conditions, and modelling the waves with the moving mesh approach as described in Section 2. Table 3 and Table 4 recap the definitions of all the test cases and the associated numeric ID (ranging from 1 to 10) to improve the readability of the plots in Section 4. In the final stage, the local-scale simulation is performed taking the mesoscale wind averaged at the second snapshot, to verify the results of the downscaling method on a different wind condition.

The computational meshes used for the local-scale simulations of Cases 1 to 8 have been generated using the blockMesh tool of the openFoam v2012 library [63]. The grid, shown in Figure 5a, is structured featuring 50×50 cells in the horizontal plane and 250 cells in the vertical direction. The first layer of cells above the ground is 0.01 m height, which amounts to $y^+ \simeq 100$.

For the phase four with the moving grid, the sea waves are modelled with the equation (7) setting an average height H_s of 1.5 m and a period T_s of 5 s, and a wavelength λ of 39 m (obtained with equation 8 for an estimated water depth on the site of 25 m). In this case a different mesh has been set up using the *cfMesh* library [64]. This is because, the

chosen wavelength requires a maximum horizontal size of the cells in contact with the water surface of about $0.5m$ to get a correct description of the waves shape. Given the size of the overall domain, a structured grid would cause an unjustifiable large number of cells and therefore, the unsteady simulation would require an unnecessary computational burden. In addition, the wave height is filtered over the sea surface according to:

$$H(r) = \begin{cases} 0, & r > r_1 \\ \frac{r-r_0}{r_1-r_0} H_s, & r_1 > r > r_0 \\ H_s, & r < r_0 \end{cases} . \tag{9}$$

where r is the distance from the OP, r_0 = 350 m and r_1 = 600 m. This choice produces two benefits: i) the waves are modelled in a sub-domain and the grid can be refined accordingly (reducing the maximum refinement region and the computational cost); ii) the mesh is not morphed close to the later boundaries (improving the numerical stability). The final mesh, shown in Figure 5b, is a Cartesian type mesh, which has the smallest elements with 0.5 m of length and 0.1 m of height, and the largest elements with side 150 m.

A 0.1 s time step value has been selected for the URANS simulations on grid 1 (Figure 5), while 0.05 s is used for the simulations with grid 2.

A grid sensitivity study has been performed to ensure that the level of refinement used for the local-scale computation guarantees mesh independent results. Proper attention must be paid to the wall distance. Indeed, in case of roughness and wall functions, a certain sensitivity to this parameter is expected. Table 1 reports the results of the grid convergence study: for each of the two different mesh topologies, the root mean square error of the wind velocity profile, relative to the fine-grid result, is shown as a function of the level of mesh refinement.

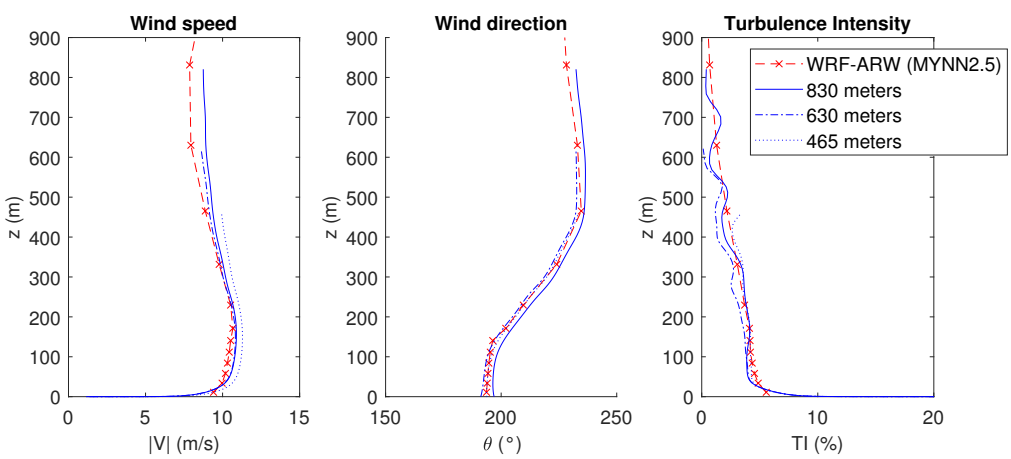

Figure 4: Comparison of different downscaling simulations varying the domain height. Test Case 1, snapshot 1 (from 10:30 to 10:40).

Grid topology	Number of cells	Average y^+	RMSE U (m/s)	RMSE Dir (°)	RMSE TKE (m^2/s^2)
1	$25 \times 25 \times 50$	172.7	0.1128	0.3193	0.04332
1	$25 \times 25 \times 100$	80.2	0.0833	0.2767	0.02228
1	$50 \times 50 \times 200$	35.6	0.0373	0.1641	0.00615
1	$100 \times 100 \times 300$	29.7	-	-	-
2	3350479	313.8 (min 76.3)	0.2962	0.4072	0.30874
2	12577954	285.8 (min 68.1)	0.0194	0.1095	0.00867
2	18889390	285.1 (min 65.4)	-	-	-

Table 1: Mesh independence study conducted for Case 1. The errors are relative to the finest grid solution per grid topology.

Case	PBL scheme		Case	PBL scheme
A	MYJ		F	UW
B	QNSE		G	GBM
C	MYNN2.5		H	EEPS
D	MYNN3.0		I	3DTKE
E	BOULAC			

Table 2: PBL schemes tested in the mesoscale simulation.

Feature / Case	Model	$(C_\mu, \sigma_k, \sigma_{(\varepsilon\|\omega)}, C_1, C_2)$
1	Steady k-ε	(0.030, 1.00, 1.30, 1.21, 1.92)[17]
2	Steady k-ε	(0.030, 1.00, 1.88, 1.44, 1.92)[18]
3	Steady k-ε	(0.090, 1.00, 1.70, 1.52, 1.833)[19]
4	Steady k-ε	(0.090, 0.74, 1.30, 1.13*, 1.90*)[20]
5	Steady k-ε	(0.15, 1.00, 1.30, 1.44*, 1.92*)[21]
6	Steady k-ω	(0.090, 1.70, 1.70, 0.52, 0.833)[19]

* The values of C_1 and C_2 should be modified above the surface layer according to [20] and [21].

Table 3: Test cases for steady local-scale simulations.

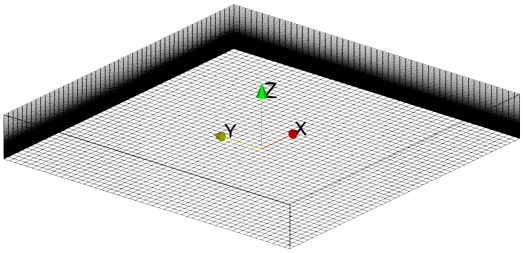

(a) blockMesh grid

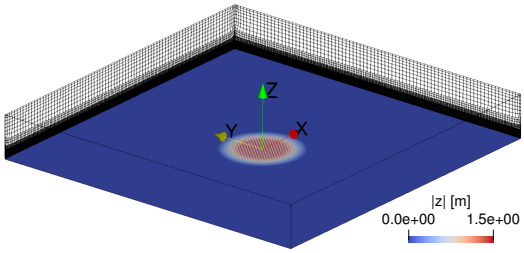

(b) cfMesh grid

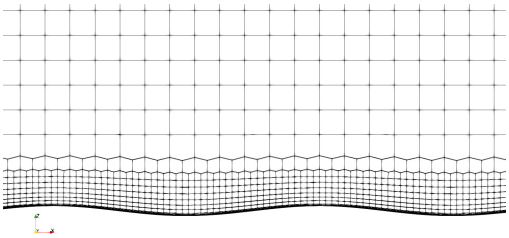

(c) cfMesh grid

Figure 5: Meshes used in the local-scale simulations.

Case \ Feature	Model	Waves	Inflow BC
7	Unsteady k-ε	-	Time-Averaged
8	Unsteady k-ε	-	Time dependent
9	Unsteady k-ε	Dynamic mesh	Time-Averaged
10	Unsteady k-ε	Dynamic mesh	Time dependent

Table 4: Test cases for unsteady local-scale simulations.

4. Results

4.1. Mesoscale analyses

The accuracy of the combined meso/local-scale prediction heavily relies on the accuracy of the mesoscale simulation. Indeed, as recalled many times in this paper, CFD can help in downscaling a given prediction to include microscale effects such as resolved ground roughness and smaller turbulence scales. However, the microscale domain is blind with respect to the weather in the surrounding area and the main features of the wind are inherited from the mesoscale simulation. For this reason, the first part of this study is aimed at screening the wind predictions obtained by WRF-ARW using 9 different PBL schemes recalled in Section 3.2.

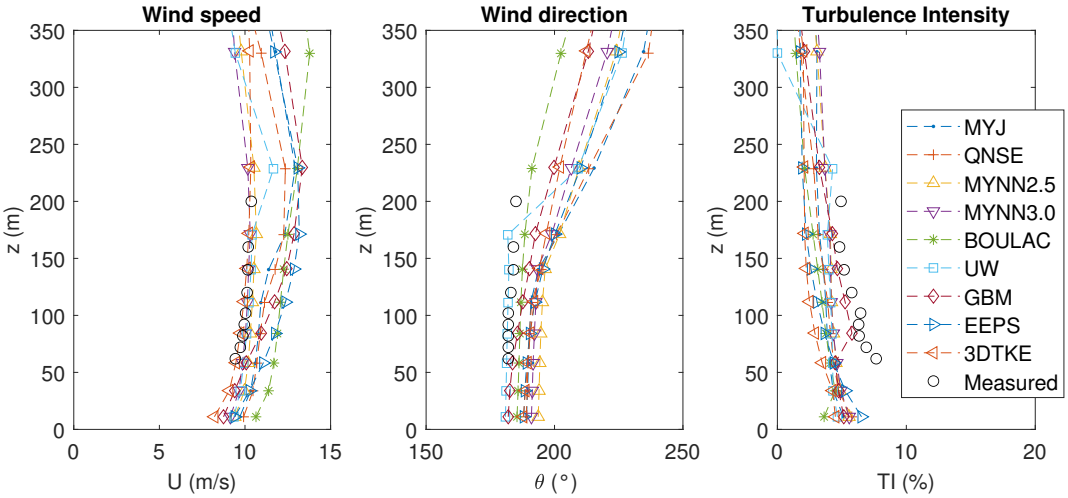

(a) Snapshot 1 (from 10:30 to 10:40)

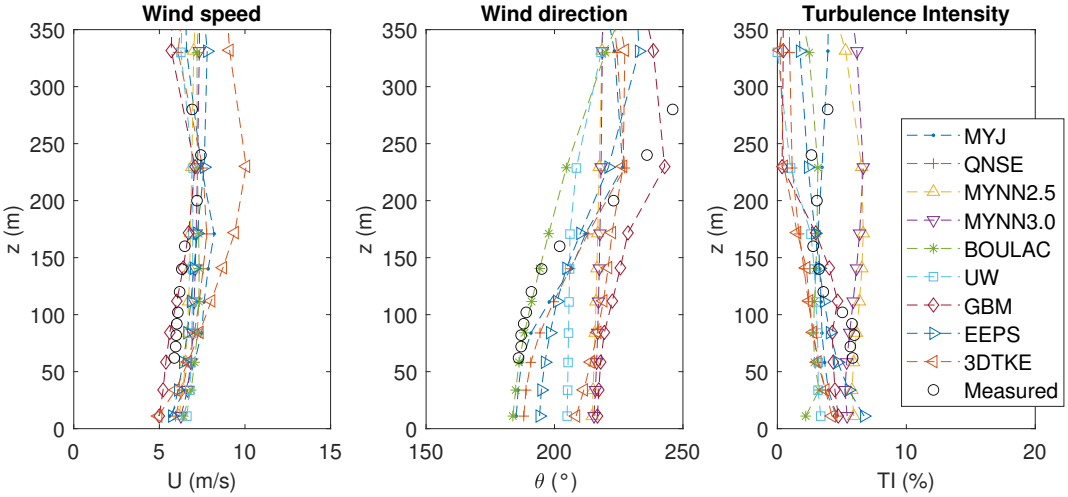

(b) Snapshot 2 (from 17:30 to 17:40)

Figure 6: PBL scheme sensitivity study.

Figure 6 reports, for the periods of tests for December 15th, 2012, the boundary layer profile of wind speed obtained with WRF-ARW using the PBL schemes of Table 2.

Figure 6a shows that, for snapshot 1, the boundary layer stability condition is near-neutral. In this condition, the prediction given by the schemes (C, D, F, I) in the first 200 m shows minimal mutual differences and it is close to the measurements. In particular, the UW scheme gives a very accurate prediction in comparison with the measurement for both velocity magnitude and direction. For $z > 170$ m, all the mesoscale simulations predict a stronger deviation of the wind direction than that effectively measured. However, the comparison can only be made in a couple of points and there is no information on the wind veer above 200 m.

In snapshot 2, the boundary layer presents a more unstable condition (Figure 6b). Here, a significant differences among the various simulations can be observed as far as the wind direction and turbulence intensity are concerned. Almost all the tested schemes over predict the velocity magnitude and under predict the wind veer. Better performance is given by schemes (E, C, D, G) for the velocity magnitude, and by schemes (E, B, A, H) for the wind direction.

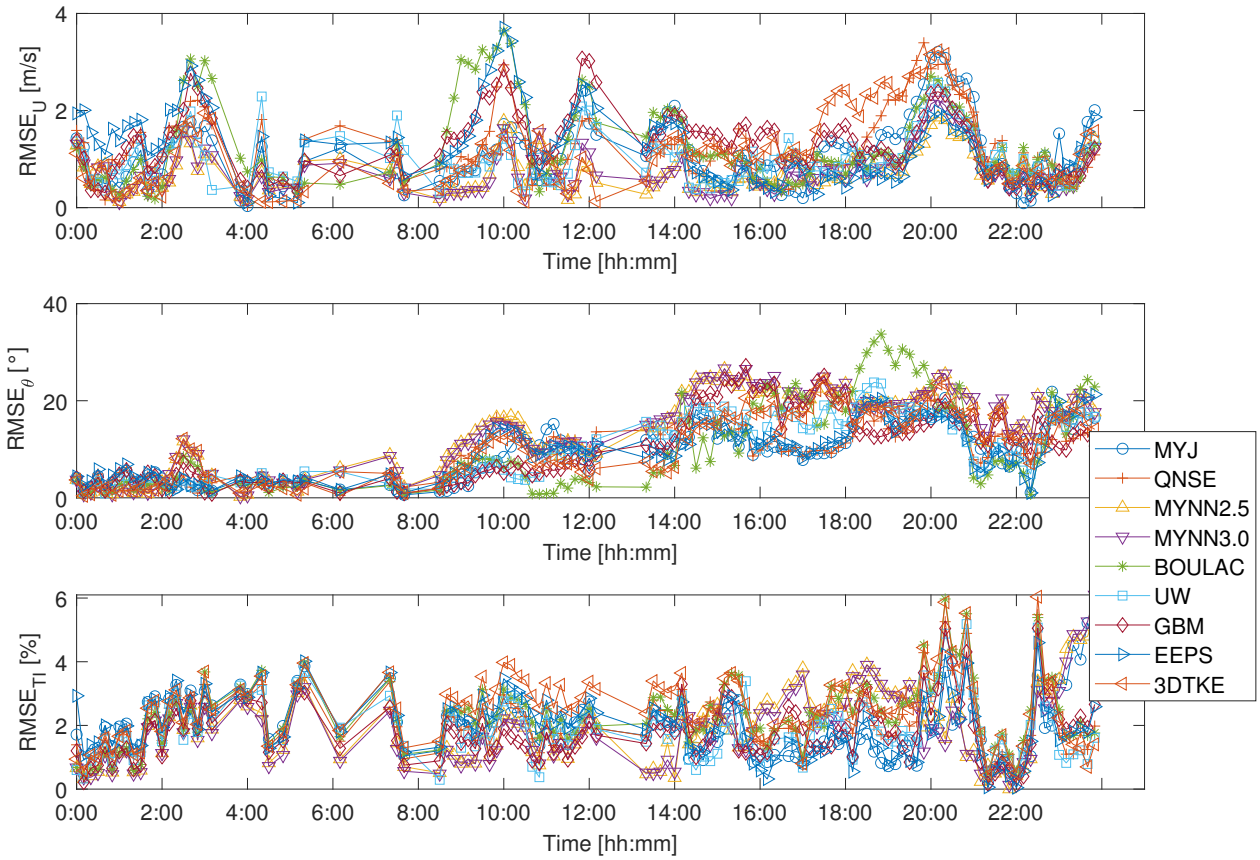

Figure 7: RMSE of WRF prediction vs. measurements of wind velocity in the first 200 m of elevation above the sea level.

Figure 7 reports the root mean squared error (RMSE) averaged along the elevation of the predictions vs. the measurements, every 10 minutes for all the 24 hours of the day. This provides a wider view of the level of accuracy of each mesoscale simulation over a long time frame.

The three plots of Figure 7 refer to the RMSE of the wind velocity, direction, and turbulent intensity. Figure 7 shows

that the accuracy of the schemes is changing throughout the day. In particular, schemes such as (C, D, F) perform better during the first part of the day, showing a generally small error, especially in wind speed. In the afternoon, the error associated with the wind velocity magnitude is higher than in the morning for all the schemes (C, D, H giving the lowest deviation from the measurements), while schemes such as (A, B, E, H) show a better agreement in terms of wind direction.

The simulation with BOULAC scheme shows the best agreement with measurements in terms of wind velocity and wind direction in Snapshot 2. It has therefore been selected to supply the boundary conditions for the local-scale simulations in Snapshot 2. In Snapshot 1, it is not possible to identify a PBL scheme which clearly outperforms the others. A slightly better agreement in terms of wind velocity, wind direction, and turbulence intensity is given by the MYNN2.5 and MYNN3.0 simulations. Therefore, the MYNN2.5 simulation has been selected for the local-scale analyses in Snapshot 1.

4.2. Combined meso/local-scale analyses

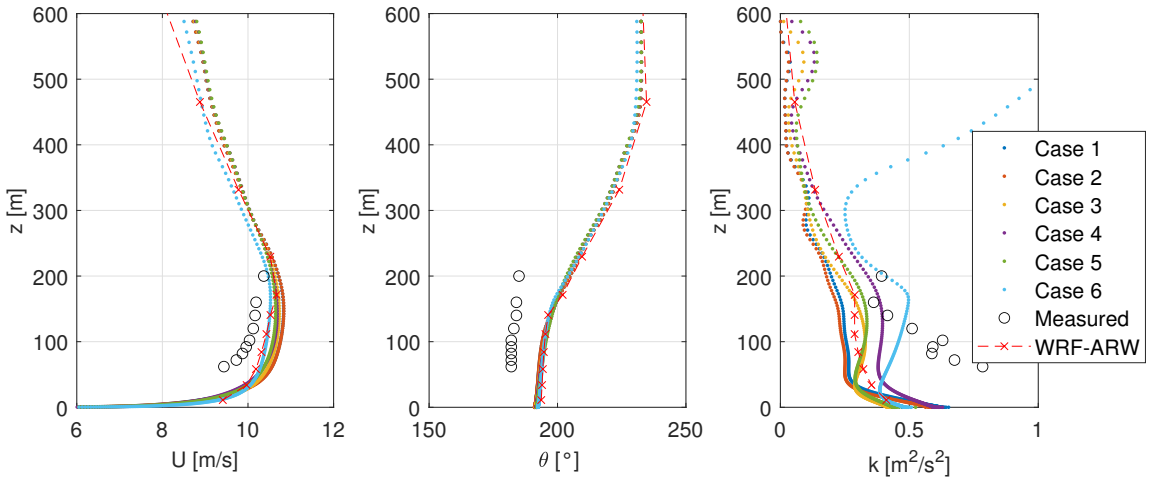

Figure 8: Downscaling results with different turbulence modelling and setups (see Table 3). Snapshot 1 (from 10:30 to 10:40).

Figure 8 reports the results of the first phase of the downscaling analyses. The results are obtained by downscaling the WRF-ARW result in the first snapshot, using the mesoscale simulation runs with the MYNN2.5 scheme. The local-scale simulation is based on the steady RANS solver, using the various turbulence model settings reported in Table 3. The plots of Figure 8 show the vertical wind profile in terms of velocity magnitude U, direction θ, and turbulent kinetic energy k. It is clear from at a first glance that the local-scale simulation preserves the velocity profile supplied by the mesoscale simulation for all the test cases, both in terms of magnitude and direction, and at all the elevations. The differences between the models can be better observed by looking at the vertical distribution of the turbulent kinetic energy, with Cases 1 and 2 showing less vertical variations and a value that, at the same height, is generally lower than the value computed in the other Cases (3 to 6). The k profile for Case 6, involving the $k-\omega$ turbulence closure, should be regarded with caution. Indeed, the profile appears visibly altered and influenced by the boundary condition

prescribed at the top patch of the domain, therefore, an in depth analysis dedicated to the sensitivity to the k and ω boundary conditions at the top surface is recommended for a correct usage of this model in future applications.

A slightly better agreement between the mesoscale prediction and the local-scale results is observed for Case 1, 3 and 5 of Table 3. Therefore, Case 1 has been selected as the baseline choice for the model constants adopted in the time dependent analyses that follow.

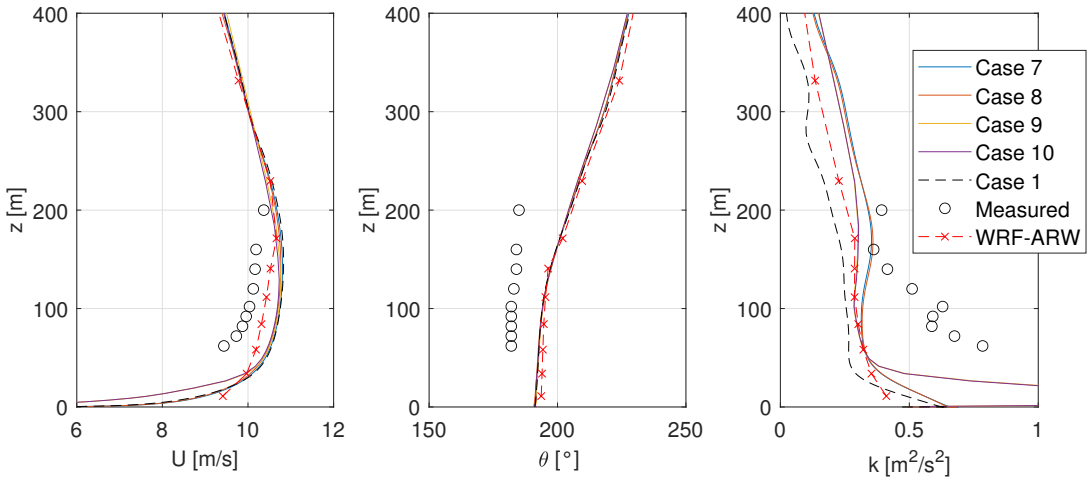

Figure 9: Downscaling with URANS. Snapshot 1 (from 10:30 to 10:40).

Figure 9 reports the comparison between the wind vertical profiles obtained with the URANS simulations (Table 4), the steady RANS simulation of Case 1, the mesoscale simulation, and the measurements in snapshot 1. A first observation is that there is not a significant difference between the average wind vertical profile obtained with the steady and unsteady RANS approaches as long as the motion of the sea-waves is not accounted for. This condition is true in both Case 7, where the boundary condition supplied by WRF is a time-averaged distribution of the quantities, and Case 8, where the time-dependent series obtained from the mesoscale simulation supply the instantaneous boundary conditions to the local-scale simulation at each time step. In contrast, there is a substantial difference between all cases analysed so far and Case 9 and 10 in the first 50 m above the sea surface. Indeed, in both cases the wave motion reduces the wind velocity in the firsts 30 to 50 m above the average sea level. This effect is probably correlated with the increase in turbulence associated to the presence and motion of the waves, as it can be seen from Figure 10a. The figure shows a perspective view of the sea surface at time t = 600 s (final time step of the simulation), along with a section of the turbulent kinetic energy field, taken within a plane parallel to the direction of waves propagation. As far as the turbulent kinetic energy profile is concerned, Figure 9 shows that, except within the first 30 m above the sea surface, the adoption of an unsteady RANS solver leads to higher levels of turbulence intensity with respect to those predicted by the steady solver.

Figure 10b shows the wind velocity vectors in a plane parallel to the direction of waves propagation, and passing through the OP. Inspection of the instantaneous velocity vectors of the wind field right above the sea surface suggests that turbulence production in the first meters above the water level is probably connected with the upwash triggered by

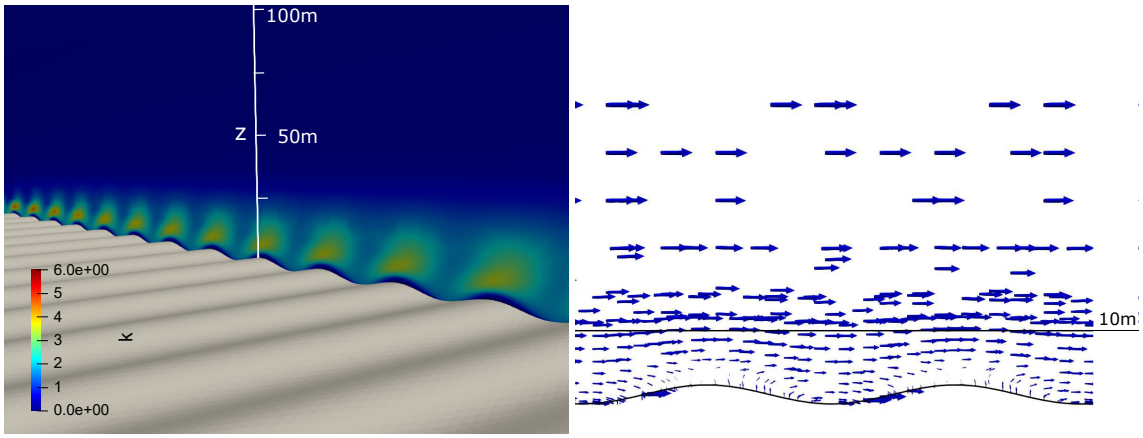

(a) k countour

(b) Velocity vectors

Figure 10: Effect of waves on the aerodynamic field above the sea surface.

the motion of the sea surface.

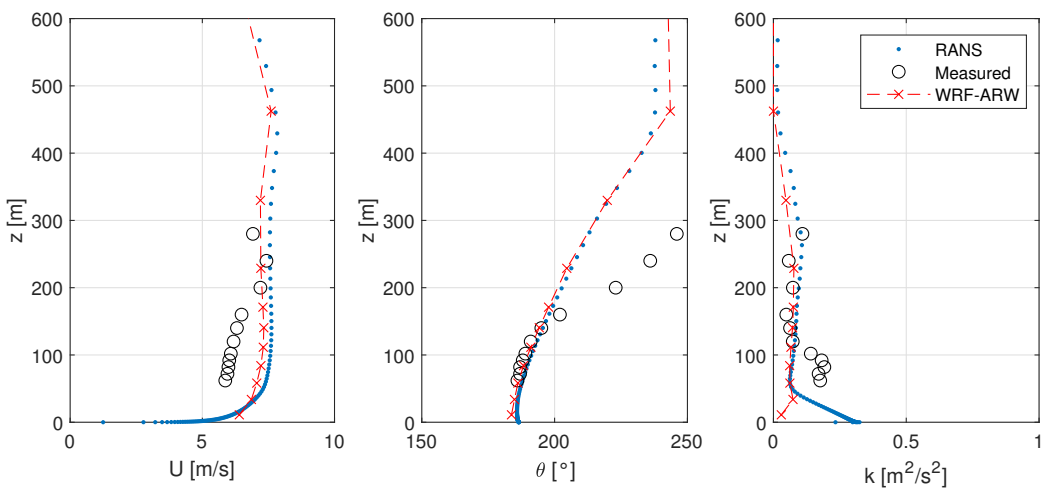

Figure 11: Downscaling results for Snapshot 2 (from 17:30 to 17:40).

Figure 11 compares the measurements in snapshot 2 against the simulated wind profile, obtained with the mesoscale simulation alone (adopting the BOULAC PBL scheme) and the combined meso/local-scale steady RANS simulation using the setup of Case 1.

Also in this case, the downscaling method faithfully preserves the wind velocity profile obtained from the mesoscale simulation, increasing the spatial resolution of the prediction in the first meters above the sea surface. A better match than for snapshot 1 can be also observed for the turbulent kinetic energy profile, which appears very close to the mesoscale prediction beyond the first 50 m. Close to the sea, the RANS simulation predicts a higher turbulence level and a stronger wind shear.

4.3. Wind turbine simulation

This final section applies the results of the former analysis, to the simulation of a bottom fixed wind turbine installed at the OP and operating for 10 minutes during the two snapshots. The turbine model used for the analysis is the IEA 15MW wind turbine [7], which represents the largest possible size for the state-of-the-art wind turbine technology. The turbine has a diameter of 240 m, and the rotor center point is located 150 m above the average sea level. With this size, the heights spanned by the blades range between 30 to 270 m, therefore we expect that a correct description of the PBL profile has a significant effect on the prediction accuracy as far as rotor performance and loads are concerned. To verify this aspect, we compare here the results of four simulations (two for each snapshot), where the turbine is operating for 10 minutes under a turbulent wind based on i) the average wind vertical profile obtained with the downscaling analyses, and ii) a theoretical wind profile obtained with the power law (PL) for the same wind velocity at the hub height and constant roughness at the sea surface. The simulations are performed with openfast.v3 [65] an aeroelastic computer-aided engineering tool for multi-body and aeroelastic simulation of horizontal axis wind turbines, developed by the National Renewable Energy Lab (NREL). The time step for all the simulations is 0.005 s, and a rigid rotor and tower are assumed, which amounts to neglect the aero-elastic effects.

The inflow wind used in the four simulations is generated with turbsim [24], an open source stochastic wind generator developed by the NREL. The wind is defined for each of the two snapshots analysed in Section 4.2 on a 31×31 grid covering the rotor swept area. The wind generator accounts for the average vertical wind profile, and for the space and time turbulent fluctuations of the wind velocity associated to the expected turbulence intensity. The turbulent fluctuations are generated automatically with the Kaimal spectral method [66] as also prescribed in the IEC61400-3 Standard. The value of the turbulence intensity for each case is obtained by averaging in space the turbulence intensity computed in the RANS simulation, in the range of elevations covered by the rotor.

The resulting time-averaged vertical profiles of the wind velocity are reported in Figure 12. Table 5 reports the values, averaged in the 10 minutes, of the wind velocity at the hub height $U_{10,HUB}$, of the turbulence intensity in the rotor area TI_{10}, of the power at the electric generator P_{10}, and of the energy produced by the turbine in the 10 minutes E_{10}. For both the wind conditions, the power and the energy produced are slightly less for the RANS wind profile. This is a consequence of the higher wind velocities that the blade faces during a revolution in the case of the exponential law profile (see Figure 12). Furthermore, we expect that the wind veer also plays a role by reducing the component of the absolute velocity which is normal to the rotor disk, with respect to a case with no veer (PL). Much larger differences can be observed in terms of blade loads. Figure 13 reports the flap-wise bending moment at the root of the blade M_y, averaged in time at all the azimuthal positions during the rotor revolution. This component of the load is the one mostly affected by the aerodynamics. Indeed, the distribution of M_y for the two types of wind profile (RANS and PL in Figure 12) are very different for both the snapshots, while the shape is qualitatively similar. The main driver is the vertical wind shear at the ground. In the case of PL, this implies a net difference of the axial velocity encountered by the blade while passing from the higher to the lower rotor semicircle (as highlighted in Figure 12). This aspect, that results in an evident shape of variation of M_y having a frequency equal to the rotor revolution frequency for the power law profile, is less pronounced in the simulated wind profiles (Figures 12a and 12b), where the convective PBL exhibits a more

Snapshot	$U_{10,HUB}$ (m/s)	TI_{10} (%)	Wind profile	P_{10} (MW)	E_{10} (MWh)
1	10.65	4.3	RANS	14.50	2.22
			PL	14.65	2.24
2	7.61	3.0	RANS	5.43	0.83
			PL	5.57	0.85

Table 5: Time-averaged data of the four openfast simulations.

uniform velocity magnitude along the heights spanned by the rotor. In the PBL case, we notice a higher average value of M_y with respect to the PL simulations, but a smaller excursion. The load shape along the revolution is probably associated to the wind veer which implies that the blade sees a positive variation of the average angle of attack when it passes through the lower rotor semicircle, and a negative variation when the blade passes in the upper rotor semicircle.

5. Concluding remarks

In this paper, we presented an extensive analysis on the use of a multiscale approach for the prediction of the wind field in an offshore site. The campaign employed numerical weather prediction (mesoscale simulation) coupled with local-scale computational fluid dynamics of turbulent flows based on the Reynolds Averaged Navier-Stokes equations, with two equation closure for the eddy viscosity model, and the Boussinesq hypothesis to account for the temperature transport and density gradients. The accuracy of the combined mesoscale/local-scale prediction of the wind vertical profile has been verified against open source LiDAR measurement for a range of heights of interest for the modern wind turbine technology. The campaign aimed at verifying the sensitivity of the prediction of the vertical wind profile using: i) 10 different TKE based PBL schemes in the WRF-ARW mesoscale simulation, ii) 6 different turbulence model settings in the RANS system, and iii) accounting also for possible dynamic effects such as time dependent wind and temperature boundary conditions, and sea waves motion.

In the final part of the work, a sample application of the proposed methodology is described, aimed at quantifying possible differences in the prediction of loads and energy output of a large scale wind turbine using two different wind profiles at the disk rotor: the one obtained using the proposed approach and one based on a semi-empirical, analytical profile.

Acknowledgment

The authors acknowledge funding support from the Italian Ministry of Education, University and Research through the Programma Operativo Nazionale Ricerca e Innovazione 2014-2020 (CUP - 34I19000050006, Activity - AIM 1859451/3). The work has been also partially performed under Project HPC-EUROPA3 (INFRAIA-2016-1-730897), with the support of the EC Research Innovation Action under the H2020 Programme; in particular, the author gratefully acknowledges the support of M. S. Campobasso from the Engineering Department at Lancaster University, and the computer resources and technical support provided by EPCC at The University of Edinburgh.

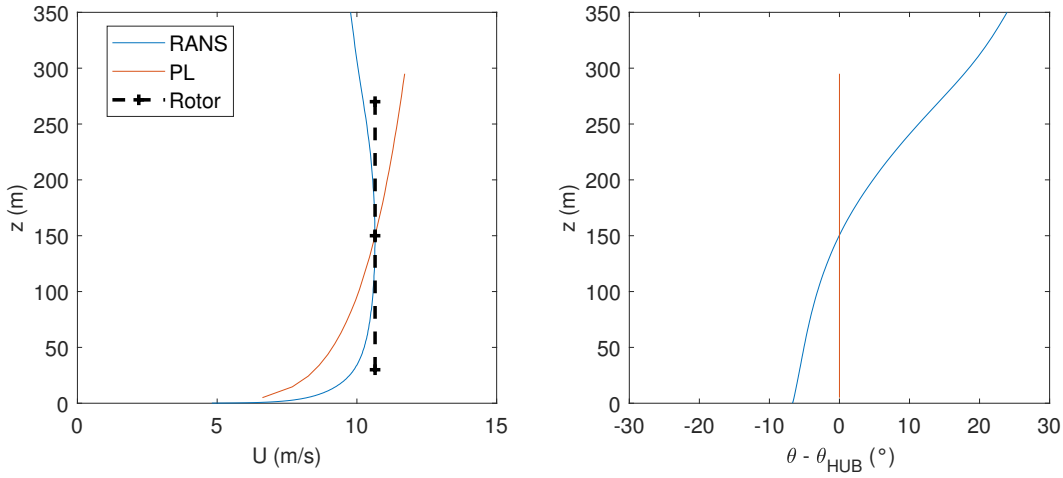

(a) Snapshot 1

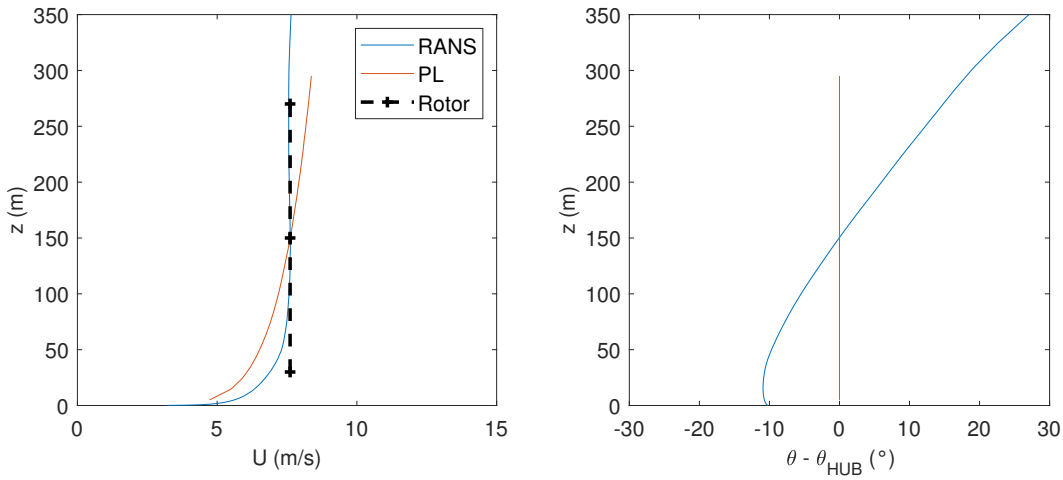

(b) Snapshot 2

Figure 12: Time averaged wind vertical profile in the openfast simulations (Blue: RANS profile, Orange: Power law).

References

[1] I. Troen and E. Lundtang Petersen. "European wind atlas", 1989.

[2] M. Tewari, H. Kusaka, F. Chen, W.J. Coirier, S. Kim, A.A. Wyszogrodzki, and T.T. Warner, "Impact of coupling a microscale computational fluid dynamics model with a mesoscale model on urban scale contaminant transport and dispersion", Atmospheric Research, **96** (2010) 656–664.

[3] S. Rafael, B. Vicente, V. Rodrigues, A. Miranda, C. Borrego, and M. Lopes, "Impacts of green infrastructures on aerodynamic flow and air quality in porto's urban area", Atmospheric Environment, **190** (2018) 317–330.

[4] B. Blocken, W. Janssen, and T. van Hooff, "Cfd simulation for pedestrian wind comfort and wind safety in

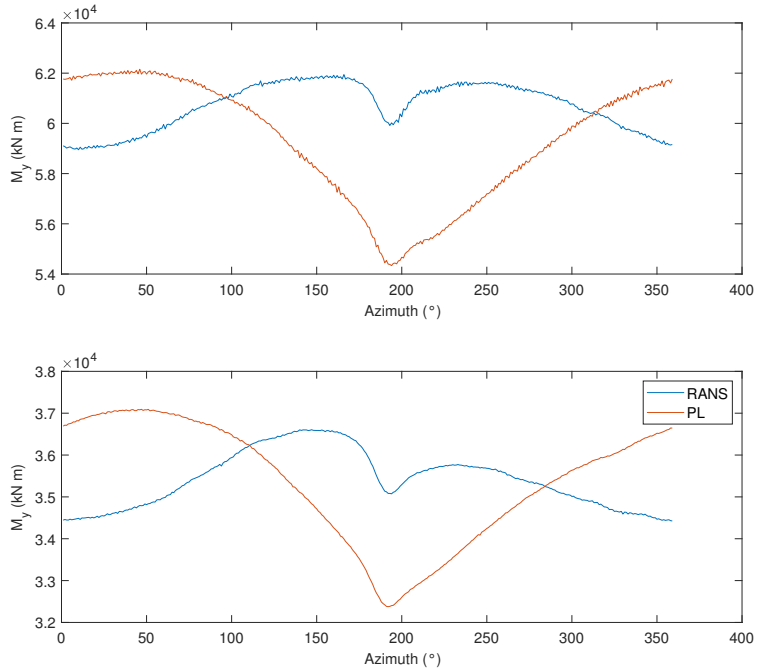

Figure 13: Time averaged flap-wise bending moment at the blade root at different azimuth positions of the blade. Top frame: snapshot 1; bottom frame: snapshot 2.

urban areas: General decision framework and case study for the eindhoven university campus", Environmental Modelling & Software, **30** (2012) 15–34.

[5] A.A. Safaei Pirooz, S. Moore, R. Turner, and R.G.J. Flay, "Coupling high-resolution numerical weather prediction and computational fluid dynamics: Auckland harbour case study", Applied Sciences, **11** (2021).

[6] L. Li and P. Chan, "Numerical simulation study of the effect of buildings and complex terrain on the low-level winds at an airport in typhoon situation", Meteorologische Zeitschrift, **21** (2012) 183.

[7] E. Gaertner, J. Rinker, L. Sethuraman, F. Zahle, B. Anderson, G. Barter, N. Abbas, F. Meng, P. Bortolotti, W. Skrzypinski, et al., "Definition of the iea wind 15-megawatt offshore reference wind turbine", Technical report, National Renewable Energy Laboratory, Golden, Mar, 2020.

[8] P. Durán, C. Meiβner, and P. Casso, "A new meso-microscale coupled modelling framework for wind resource assessment: A validation study", Renewable Energy, **160** (2020) 538–554.

[9] P. Durán, C. Meißner, K. Rutledge, R. Fonseca, J. Martin-Torres, and M.S. Adaramola, "Meso-microscale coupling for wind resource assessment using averaged atmospheric stability conditions", Meteorologische Zeitschrift, **28** (2019) 273–291, doi: 10.1127/metz/2019/0937.

[10] V.J. Duraisamy, E. Dupont, and B. Carissimo, "Downscaling wind energy resource from mesoscale to microscale

model and data assimilating field measurements", Journal of Physics: Conference Series, **555** (2014) 012031, doi: 10.1088/1742-6596/555/1/012031.

[11] A. Castorrini, S. Gentile, E. Geraldi, and A. Bonfiglioli, "Increasing spatial resolution of wind resource prediction using nwp and rans simulation", Journal of Wind Engineering and Industrial Aerodynamics, **210** (2021) 104499.

[12] D. Leukauf, A. El-Bahlouli, K. zum Berge, M. Schön, H. Knaus, and J. Bange, "The impact of a forest parametrization on coupled wrf-cfd simulations during the passage of a cold front over the winsent test-site", Wind Energy Science Discussions, **2019** (2019) 1–24.

[13] J.S. Rodrigo, P. Santos, R.C. Arroyo, M. Avila, D. Cavar, O. Lehmkuhl, H. Owen, R. Li, and E. Tromeur, "The alex17 diurnal cycles in complex terrain benchmark", in Journal of Physics: Conference Series, number 1. IOP Publishing, (2021) 012002.

[14] Y. Liu, S. Miao, C. Zhang, G. Cui, and Z. Zhang, "Study on micro-atmospheric environment by coupling large eddy simulation with mesoscale model", Journal of Wind Engineering and Industrial Aerodynamics, **107-108** (2012) 106–117, doi: https://doi.org/10.1016/j.jweia.2012.03.033.

[15] A.A. Wyszogrodzki, S. Miao, and F. Chen, "Evaluation of the coupling between mesoscale-wrf and les-eulag models for simulating fine-scale urban dispersion", Atmospheric Research, **118** (2012) 324–345.

[16] P. Richards and R. Hoxey, "Appropriate boundary conditions for computational wind engineering models using the k-epsilon turbulence model", Journal of wind engineering and industrial aerodynamics, **46** (1993) 145–153.

[17] A. Bechmann and N.N. Sørensen, "Hybrid rans/les method for wind flow over complex terrain", Wind Energy: An International Journal for Progress and Applications in Wind Power Conversion Technology, **13** (2010) 36–50.

[18] G.G. Katul, L. Mahrt, D. Poggi, and C. Sanz, "One-and two-equation models for canopy turbulence", Boundary-layer meteorology, **113** (2004) 81–109.

[19] A. Sogachev, M. Kelly, and M.Y. Leclerc, "Consistent two-equation closure modelling for atmospheric research: buoyancy and vegetation implementations", Boundary-layer meteorology, **145** (2012) 307–327.

[20] H. Detering and D. Etling, "Application of the e-ε turbulence model to the atmospheric boundary layer", Boundary-Layer Meteorology, **33** (1985) 113–133.

[21] O. Temel, S. Porchetta, L. Bricteux, and J. van Beeck, "Rans closures for non-neutral microscale cfd simulations sustained with inflow conditions acquired from mesoscale simulations", Applied Mathematical Modelling, **53** (2018) 635–652.

[22] O. Temel, L. Bricteux, and J. van Beeck, "Coupled wrf-openfoam study of wind flow over complex terrain", Journal of Wind Engineering and Industrial Aerodynamics, **174** (2018) 152–169.

[23] Ørsted Open Data Service. Available online: https://orsted.com/en/our-business/offshore-wind/wind-data, Accessed on 12 March 2021.

[24] B.J. Jonkman, "Turbsim user's guide: Version 1.50", Technical report, National Renewable Energy Lab.(NREL), Golden, CO (United States), 2009.

[25] W.C. Skamarock, J.B. Klemp, J. Dudhia, D.O. Gill, D.M. Barker, W. Wang, and J.G. Powers, "A description of the advanced research wrf version 3. ncar technical note-475+ str", Technical report, NCAR, 2008.

[26] W.C. Skamarock, J.B. Klemp, J. Dudhia, D.O. Gill, Z. Liu, J. Berner, W. Wang, J.G. Powers, M.G. Duda, D.M. Barker, et al., "A description of the advanced research wrf model version 4.3", Technical Report NCAR/TN-556+STR, Natl. Ctr. Atmos. Res., Boulder, CO, 2021, doi:10.5065/1dfh-6p97.

[27] W. Wang, C. Bruyère, M. Duda, J. Dudhia, D. Gill, M. Kavulich, K. Keene, M. Chen, H. Lin, J. Michalakes, et al., "Wrf-arw version 3 modeling system user's guide", Technical report, National Centre for Atmospheric Research, 2009.

[28] V. Lara-Fanego, J. Ruiz-Arias, D. Pozo-Vázquez, F. Santos-Alamillos, and J. Tovar-Pescador, "Evaluation of the wrf model solar irradiance forecasts in andalusia (southern spain)", Solar Energy, **86** (2012) 2200–2217.

[29] R. Perez and T. Hoff, "Solar anywhere forecasting", Solar Energy Forecasting and Resource Assessment. Elsevier, (2013).

[30] E. Lorenz, J. Remund, S.C. Müller, W. Traunmüller, G. Steinmaurer, D. Pozo, J. Ruiz-Arias, V.L. Fanego, L. Ramirez, M.G. Romeo, et al., "Benchmarking of different approaches to forecast solar irradiance", in 24th European photovoltaic solar energy conference. Hamburg, Germany, (2009) 21–25.

[31] T.L. Feudo, E. Avolio, D. Gullì, S. Federico, C.R. Calidonna, and A.M. Sempreviva, "Comparison of hourly solar radiation from a ground–based station, remote sensing and weather forecast models at a coastal site of south italy (lamezia terme)", Energy Procedia, **76** (2015) 148–155.

[32] S. Gentile, F. Di Paola, D. Cimini, D. Gallucci, E. Geraldi, S. Larosa, S.T. Nilo, E. Ricciardelli, E. Ripepi, M. Viggiano, et al., "3d-var data assimilation of seviri radiances for the prediction of solar irradiance in italy using wrf solar mesoscale model—preliminary results", Remote Sensing, **12** (2020) 920.

[33] D. Carvalho, A. Rocha, M. Gómez-Gesteira, and C.S. Santos, "Wrf wind simulation and wind energy production estimates forced by different reanalyses: Comparison with observed data for portugal", Applied Energy, **117** (2014) 116–126.

[34] S. Shimada and T. Ohsawa, "Accuracy and characteristics of offshore wind speeds simulated by wrf", Sola, **7** (2011) 21–24.

[35] D. Carvalho, A. Rocha, M. Gómez-Gesteira, and C. Santos, "A sensitivity study of the wrf model in wind simulation for an area of high wind energy", Environmental Modelling & Software, **33** (2012) 23–34.

[36] R.B. Bird, W.E. Stewart, and E.N. Lightfoot, "Transport phenomena john wiley & sons", New York, **413** (1960).

[37] B.E. Launder and D.B. Spalding, "The numerical computation of turbulent flows", in Numerical prediction of flow, heat transfer, turbulence and combustion, 96–116, Elsevier, 1983.

[38] F.R. Menter, M. Kuntz, and R. Langtry, "Ten years of industrial experience with the sst turbulence model", Turbulence, heat and mass transfer, **4** (2003) 625–632.

[39] M. Alletto, A. Radi, J. Adib, J. Langner, C. Peralta, A. Altmikus, and M. Letzel, "E-wind: Steady state cfd approach for stratified flows used for site assessment at enercon", in Journal of Physics: Conference Series, number 7. IOP Publishing, (2018) 072020.

[40] D.D. Apsley and I.P. Castro, "A limited-length-scale k-ε model for the neutral and stably-stratified atmospheric boundary layer", Boundary-layer meteorology, **83** (1997) 75–98.

[41] B. Blocken and J. Carmeliet, "Modelling atmospheric-boundary-layer flow with fluent: curing the wall-function roughness incompatibility.", in conference; Fluent Benelux 2004 User Group Meeting; 2004-10-05; 2004-10-06, (2004).

[42] D. Hargreaves and N.G. Wright, "On the use of the k–ε model in commercial cfd software to model the neutral atmospheric boundary layer", Journal of wind engineering and industrial aerodynamics, **95** (2007) 355–369.

[43] H. Charnock, "Wind stress on a water surface", Quarterly Journal of the Royal Meteorological Society, **81** (1955) 639–640.

[44] J.A. Bye and J.-O. Wolff, "Charnock dynamics: a model for the velocity structure in the wave boundary layer of the air–sea interface", Ocean Dynamics, **58** (2008) 31–42.

[45] S. Porchetta, D. Muñoz-Esparza, W. Munters, J. van Beeck, and N. van Lipzig, "Impact of ocean waves on offshore wind farm power production", Renewable Energy, **180** (2021) 1179–1193, doi: https://doi.org/10.1016/j.renene.2021.08.111.

[46] P.P. Sullivan, J.C. McWilliams, and E.G. Patton, "Large-eddy simulation of marine atmospheric boundary layers above a spectrum of moving waves", Journal of the Atmospheric Sciences, **71** (2014) 4001–4027.

[47] H. Jasak, "Dynamic mesh handling in openfoam", in 47th AIAA aerospace sciences meeting including the new horizons forum and aerospace exposition, (2009) 341.

[48] J. Davidson, M. Karimov, A. Szelechman, C. Windt, and J. Ringwood, "Dynamic mesh motion in openfoam for wave energy converter simulation", in 14th OpenFOAM Workshop, (2019).

[49] Y. Goda, Random seas and design of maritime structures, volume 33. World Scientific Publishing Company, 2010.

[50] Y. Yang, M. Gu, S. Chen, and X. Jin, "New inflow boundary conditions for modelling the neutral equilibrium atmospheric boundary layer in computational wind engineering", Journal of Wind Engineering and Industrial Aerodynamics, **97** (2009) 88–95.

[51] F.R.P. in the Baltic Sea. Available online: `https://www.fino2.de/en/`.

[52] G. Thompson and T. Eidhammer, "A study of aerosol impacts on clouds and precipitation development in a large winter cyclone", Journal of the atmospheric sciences, **71** (2014) 3636–3658.

[53] E.J. Mlawer, S.J. Taubman, P.D. Brown, M.J. Iacono, and S.A. Clough, "Radiative transfer for inhomogeneous atmospheres: Rrtm, a validated correlated-k model for the longwave", Journal of Geophysical Research: Atmospheres, **102** (1997) 16663–16682.

[54] J. Dudhia, "Numerical study of convection observed during the winter monsoon experiment using a mesoscale two-dimensional model", Journal of the atmospheric sciences, **46** (1989) 3077–3107.

[55] C.W. Fairall, E.F. Bradley, J.E. Hare, A.A. Grachev, and J.B. Edson, "Bulk parameterization of air–sea fluxes: Updates and verification for the coare algorithm", Journal of Climate, **16** (2003) 571 – 591, doi: 10.1175/1520-0442(2003)016¡0571:BPOASF¿2.0.CO;2.

[56] M. Ek, K. Mitchell, Y. Lin, E. Rogers, P. Grunmann, V. Koren, G. Gayno, and J. Tarpley, "Implementation of noah land surface model advances in the national centers for environmental prediction operational mesoscale eta model", Journal of Geophysical Research: Atmospheres, **108** (2003).

[57] Z.I. Janjić, "The step-mountain eta coordinate model: Further developments of the convection, viscous sublayer, and turbulence closure schemes", Monthly weather review, **122** (1994) 927–945.

[58] S. Sukoriansky, B. Galperin, and V. Perov, "Application of a new spectral theory of stably stratified turbulence to the atmospheric boundary layer over sea ice", Boundary-layer meteorology, **117** (2005) 231–257.

[59] P. Bougeault and P. Lacarrere, "Parameterization of orography-induced turbulence in a mesobeta–scale model", Monthly weather review, **117** (1989) 1872–1890.

[60] C.S. Bretherton and S. Park, "A new moist turbulence parameterization in the community atmosphere model", Journal of Climate, **22** (2009) 3422–3448.

[61] H. Grenier and C.S. Bretherton, "A moist pbl parameterization for large-scale models and its application to subtropical cloud-topped marine boundary layers", Monthly weather review, **129** (2001) 357–377.

[62] J.W. Deardorff, "Stratocumulus-capped mixed layers derived from a three-dimensional model", Boundary-layer meteorology, **18** (1980) 495–527.

[63] H.G. Weller, G. Tabor, H. Jasak, and C. Fureby, "A tensorial approach to computational continuum mechanics using object-oriented techniques", Computers in physics, **12** (1998) 620–631.

[64] F. Juretic, “cfmesh user guide”, Creative Fields, Ltd, **1** (2015).

[65] J. Jonkman and M. Sprague, “Openfast: An aeroelastic computer-aided engineering tool for horizontal axis wind turbines”, National Renewable Energy Laboratory, Golden, CO, accessed Mar, **17** (2020).

[66] J.C. Kaimal, J. Wyngaard, Y. Izumi, and O. Coté, “Spectral characteristics of surface-layer turbulence”, Quarterly Journal of the Royal Meteorological Society, **98** (1972) 563–589.